Check for updates

# Integration of a Cu₂O/ZnO heterojunction and Ag@SiO₂ into a photoanode for enhanced solar water oxidation†

Xuyang Zeng,[ab] Qianyu Gao,[ab] Peilin Song,[b] Xinru Zhang,[b] Jiaying Xie,[b] Qingwen Dong,[b] Junjie Qi,[b] Xiu-Shuang Xing [ID] *[b] and Jimin Du*[ab]

Photoelectrochemical water splitting (PEC-WS) has attracted considerable attention owing to its low energy consumption and sustainable nature. Constructing semiconductor heterojunctions with controllable band structure can effectively facilitate photogenerated carrier separation. In this study, a FTO/ZnO/Cu₂O/Ag@SiO₂ photoanode with a Cu₂O/ZnO p–n heterojunction and Ag@SiO₂ nanoparticles is constructed to investigate its PEC-WS performance. Compared with a bare ZnO photoanode, the photocurrent density of the FTO/ZnO/Cu₂O/Ag@SiO₂ photoanode (0.77 mA cm$^{-2}$) at 1.23 V$_{RHE}$ exhibits an increment of 88%, and a cathodic shift of 0.1 V for the on-set potential (0.4 V$_{RHE}$). Detailed photoelectrochemical analyses reveal that the Cu₂O/ZnO p–n heterojunction formed between Cu₂O and ZnO can effectively promote photogenerated carrier separation. The surface plasmonic effect of the Ag@SiO₂ nanoparticles can further promote the photogenerated carrier transfer efficiency, which synergistically improves the PEC-WS performance.

## Introduction

With rapid technological and industrial advances, environmental pollution and the energy crisis have become urgent issues. Developing clean and sustainable energy is crucial to alleviate this crisis.[1] Photoelectrochemical water splitting (PEC-WS) has attracted extensive research attention because it can be a low-cost, renewable and environmentally friendly method for hydrogen production.[2,3] Various metal oxide semiconductor materials, such as TiO₂,[4] ZnO,[5] α-Fe₂O₃,[6] and BiVO₄,[7] have been widely applied to investigate their PEC-WS performances. Among these, ZnO is an n-type semiconductor with a band gap energy of ~3.3 eV, which exhibits a suitable band position and high electron mobility, and can be considered as one of the popular semiconductor materials in the photocatalysis field.[8–11] However, its further applications are limited to the rapid recombination of photogenerated carriers and low utilization of visible light.[12]

Various methods, such as metal doping, surface catalysts, and heterojunction construction, are applied to improve the

photoelectric conversion efficiency of ZnO.[13–15] The construction of heterojunctions is one of the effective methods to improve PEC-WS performance and also attracts widespread attention.[16] Z-type heterojunctions can provide a stable internal electric field between semiconductors and accelerate the migration of photogenerated carrier, which are preferred over general heterojunctions.[17–19] For instance, Li *et al.* prepared a semiconductor with a ZnO/ZnS heterojunction by ion exchange sulfidation treatment, and found the photocurrent density was 1.35 times that of the bare ZnO photoanode at 1.23 V$_{RHE}$.[20] Maity *et al.* synthesized n-ZnO/p-ZnCo₂O₄ photoanodes with heterojunctions, in which the introduction of ZnCo₂O₄ decreased surface defects, inhibited the recombination of photogenerated carrier, and increased the photocurrent density of ZnO photoanodes.[21,22]

In this study, ZnO photoanodes with nanosheet-like structures are prepared by a hydrothermal method, where Cu₂O is introduced on the surface of ZnO to construct a Cu₂O/ZnO p–n heterojunction structure. The FTO/ZnO/Cu₂O/Ag@SiO₂ photoanode exhibits a maximum photocurrent density of 0.77 mA cm$^{-2}$ at 1.23 V$_{RHE}$, which increases by 88% compared with the bare FTO/ZnO photoanode. This is mainly attributed to the p–n heterojunction formed between Cu₂O and ZnO, which effectively promotes the separation and transfer efficiency of photogenerated carrier. The introduction of Ag@SiO₂ catalyst further increases the transfer efficiency of photogenerated electrons and holes *via* the surface plasmonic effect.

*[a]College of Chemistry, Zhengzhou University, Zhengzhou 450000, P. R. China. E-mail: djm@iccas.ac.cn*

*[b]Henan Key Laboratory of New Optoelectronic Functional Materials, College of Chemistry and Chemical Engineering, Anyang Normal University, Anyang 455000, P. R. China. E-mail: xsxing0621@163.com*

† Electronic supplementary information (ESI) available. See DOI: https://doi.org/10.1039/d3ra07738a

## Experimental

### Preparing FTO/ZnO photoanodes

The ingredients and reagents used herein were purchased and used directly without additional purification. FTO conductive glass was ultrasonically cleaned with acetone, ethanol, and deionized water for 15 min, successively. The FTO substrate was obliquely placed in a Teflon reactor, where its conductive side was facing down. ZnOOH films were prepared using the hydrothermal method: 0.4998 g $Zn(NO_3)_2$ and 0.5043 g urea were dissolved in 60 mL distilled water. This solution was poured into the Teflon reactor and heated in an oven for 7 h at 100 °C. A white ZnOOH film was clearly observed on the FTO glass, and it was labeled as FTO/ZnOOH. This was further annealed at 500 °C for 2 h to prepare the FTO/ZnO photoanode.

### Preparing FTO/ZnO/Cu₂O nanorod arrays

Copper sulfate (3.1922 g) and sodium thiosulfate (19.85 g) were separately dissolved in 20 mL and 80 mL of distilled water, respectively. Then, they were placed ultrasonically together for 15 min to obtain a mixed solution. Sodium hydroxide (2 g) was dissolved in 100 mL distilled water. The prepared FTO/ZnO nanorods were immersed in the above mixed solution for 2 s, distilled water for 30 s, an aqueous NaOH solution at 70 °C for 2 s, and finally distilled water for 30 s. The above deposition reaction process constituted one cycle. FTO/ZnO nanorods were treated through one, two and three cycles, and denoted as FTO/ZnO/Cu₂O-1, FTO/ZnO/Cu₂O-2, and FTO/ZnO/Cu₂O-3, respectively. Because of the optimal photoelectrochemical conversion for FTO/ZnO/Cu₂O-2 photoanode, the following modifications with Ag and Ag@SiO₂ were all based on it. Hereafter, the FTO/ZnO/Cu₂O-2 photoanode was also denoted as the FTO/ZnO/Cu₂O photoanode.

### Preparing FTO/ZnO/Cu₂O/Ag and FTO/ZnO/Cu₂O/Ag@SiO₂

A mixed silver nitrate (13.25 mmol, 200 mL) and sodium citrate (100 mmol, 1.94 mL) aqueous solution were boiled for 15 min, and cooled to 25 °C to obtain a silver colloidal solution. The silver colloidal solution was centrifuged at 1000 rpm and then washed sequentially with deionized water and ethanol.[22] Finally, the prepared AgNPs and ethanol were dispersed on FTO/ZnO/Cu₂O to obtain the FTO/ZnO/Cu₂O/Ag photoanode.

Furthermore, 25 mL of an ethanol solution containing AgNPs was diluted with ethanol to obtain a 100 mL solution.

Then 3 mL of ammonia was added to this solution, and ultrasonicated for 30 min. 10 μL of tetraethyl orthosilicate was added to the above mixed solution, stirred at 30 °C, centrifuged for 10 min to obtain Ag@SiO₂-NPs, and finally washed in turn with deionized water and ethanol.[22] FTO/ZnO/Cu₂O/Ag@SiO₂ was obtained by dispersing Ag@SiO₂-NPs and ethanol in FTO/ZnO/Cu₂O (Scheme 1).

### Structure characterization

The surface morphology of ZnO photoanodes was investigated using field-emission scanning electron microscopy (SEM, Quanta 400 FEG and Hitachi S4800), and the micromorphology and elemental composition were characterized using transmission electron microscopy (TEM, FEI Talos F200X) coupled with elements line scanning and energy-dispersive X-ray spectroscopy (EDS). X-ray diffraction (XRD) spectra were recorded using X'Pert Pro MPD (Cu $K\alpha$ radiation). X-ray photoelectron spectroscopy (XPS) was performed on a Thermo ESCALAB 250Xi spectrometer to analyze the surface chemical state and elemental composition of photoanodes. UV-vis spectra were analyzed using UV 3600 Shimadzu.

### PEC-WS measurement

Photoelectrochemical measurements were performed on an electrochemical workstation (CHI 660E) with a three-electrode test system (i.e., the prepared ZnO photoanode as the working electrode, Ag/AgCl as the reference electrode, and Pt as the counter electrode). The electrolyte was a 1.0 M NaOH aqueous solution. A simulated sunlight (CEL-HXF3-T3), with a normal power density of 100 mW cm$^{-2}$ and an AM 1.5 G filter, was selected as the light source. Photocurrent density–voltage ($J$–$V$) curves were measured from negative potential to positive potential with a sweep speed of 20 mV s$^{-1}$. Mott–Schottky plots were measured at 1 kHz under dark conditions. Electrochemical impedance spectroscopy (EIS) was conducted under simulated sunlight at 1.23 $V_{RHE}$ from 0.1 Hz to 100 kHz.

## Results and discussion

The SEM images show that the ZnO film composes of nanosheets with ~5 nm thickness (Fig. 1a and b). A few Cu₂O nanoparticles grow on the surface of FTO/ZnO photoanode, and the thickness of Cu₂O nanoparticles increases with the increased deposition circles (Fig. S1†). The ZnO film maintains
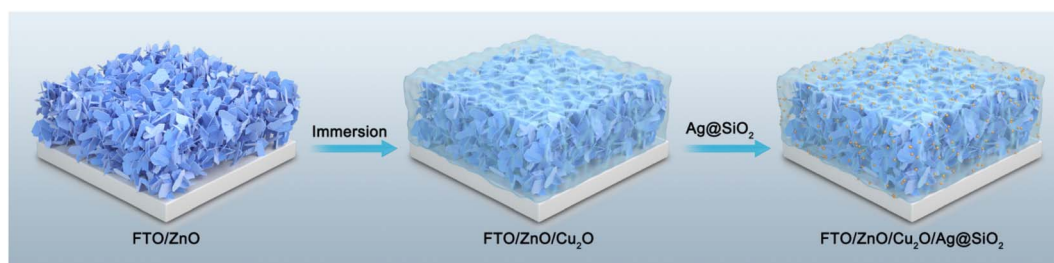


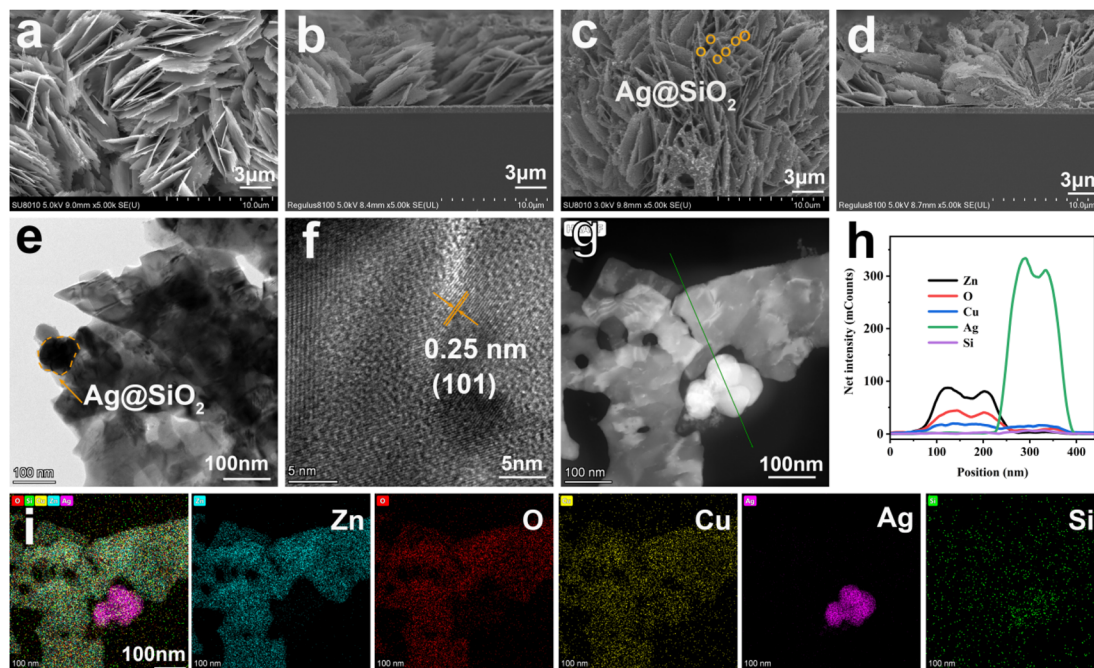Scheme 1  The schematic preparation procedure of FTO/ZnO/Cu₂O/Ag@SiO₂ photoanode.

**Fig. 1** SEM images of FTO/ZnO (a and b) and FTO/ZnO/Cu$_2$O/Ag@SiO$_2$ (c and d); (a and c are the top-view images, b and d are the cross-sectional images); (e) TEM, (f) HR-TEM, (g–h) elements linear scanning images of FTO/ZnO/Cu$_2$O/Ag@SiO$_2$; (i) EDS elements mapping images of FTO/ZnO/Cu$_2$O/Ag@SiO$_2$ photoanodes.

the nanosheet shape after the introduction of Cu$_2$O. The characterization peak of ZnO in the XRD spectra keeps almost unchanged (Fig. S2†), indicating that the introduction of Cu$_2$O has no effect on the ZnO film. The ZnO photoanode modified by Cu$_2$O exhibits an obvious UV-vis absorbance enhancement at 250~400 nm, where the FTO/ZnO/Cu$_2$O-2 photoanode possesses the best light absorption capacity (Fig. S3†).

As shown in the SEM images of Fig. 1c and d, the FTO/ZnO and FTO/ZnO/Cu$_2$O/Ag@SiO$_2$ photoanodes all possess a similar nanosheet-like structure, which are closely arranged. This structural character of vertical nanosheets provides favorable bars for the formation of p–n heterojunctions. Many Ag@SiO$_2$ nanoparticles are accumulated on the surface of the FTO/ZnO/Cu$_2$O photoanode with a thickness of ~5 nm (Fig. 1c). TEM is conducted to investigate the morphological changes in the photoanodes after introducing Ag@SiO$_2$ catalysts (Fig. 1e). The inter-planar distances of 0.25 nm in the shell region match well with the lattice fringes of (101) planes of ZnO (Fig. 1f). ZnO is presented as a nanosheet with a diameter of ~50 nm modified with Cu$_2$O and Ag@SiO$_2$ nanoparticles. EDS data proves the successful introduction of Ag@SiO$_2$ nanoparticles on the surface of FTO/ZnO/Cu$_2$O photoanode (Fig. 1g–i). XRD patterns show that the peak positions of FTO/ZnO/Cu$_2$O/Ag and FTO/ZnO/Cu$_2$O/Ag@SiO$_2$ photoanodes are almost the same as that of the pure ZnO photoanode (Fig. S4†), indicating that the introduction of Ag and Ag@SiO$_2$ nanoparticles cannot cause the phase transition of ZnO photoanodes.[23] In the UV-vis absorption spectra, the absorption edge of each photoanode is ~400 nm (Fig. S5†). The absorbance intensities of FTO/ZnO/Cu$_2$O/Ag and FTO/ZnO/Cu$_2$O/Ag@SiO$_2$ photoanodes are all

stronger than that of the FTO/ZnO photoanode, which can be attributed to the formation of a heterojunction in the interface of ZnO and Cu$_2$O and the introduced Ag and Ag@SiO$_2$ catalysts.[24]

XPS is used for surface chemical state and elemental analyses, which proves the existence of elemental Zn, Cu, O, Ag, and Si in the FTO/ZnO/Cu$_2$O/Ag@SiO$_2$ photoanode (Fig. S6†). Zn 2p has two main peaks at 1022.1 eV and 1045 eV (Fig. 2a). Spin orbital splitting is also observed in Zn 2p signals, demonstrating the presence of Zn$^{2+}$ in ZnO.[25] The O 1s spectrum mainly consists of two peaks of 531.8 eV (oxygen defect) and 530.3 eV (lattice oxygen). The oxygen vacancy intensity of FTO/ZnO/Cu$_2$O/Ag photoanode becomes slightly lower, indicating fewer surface defects. The lattice oxygen intensity of FTO/ZnO/Cu$_2$O/Ag@SiO$_2$ photoanode is relatively higher, indicating that its surface crystallinity is excellent. After introducing the Cu$_2$O and Ag@SiO$_2$ catalysts, the $O_v$ peak moves in a lower binding energy, which is conducive to carrier transfer (Fig. 2b).[26] The ~933.7 eV and ~953.4 eV of Cu 2p can be attributed to Cu 2p$_{3/2}$ and Cu 2p$_{1/2}$, indicating the presence of Cu$_2$O in the photoanodes (Fig. 2c).[27,28] The two peaks of Ag 3d$_{1/2}$ (~373.9 eV) and Ag 3d$_{3/2}$ (~367.8 eV) also further prove the presence of elemental Ag (Fig. 2d).[29] The XRD patterns are conducted to recognize the phase of ZnO, Cu$_2$O, Ag and SiO$_2$ in the FTO/ZnO/Cu$_2$O/Ag@SiO$_2$ photoanode, but the Cu$_2$O and Ag@SiO$_2$ films are too thin to find their characteristic peaks. The presence of Cu$_2$O and Ag@SiO$_2$ are proved mainly by XPS and elemental analysis.[30]

The linear scanning voltammetry, transient photocurrent curves, EIS, and Mott–Schottky measurements are conducted to
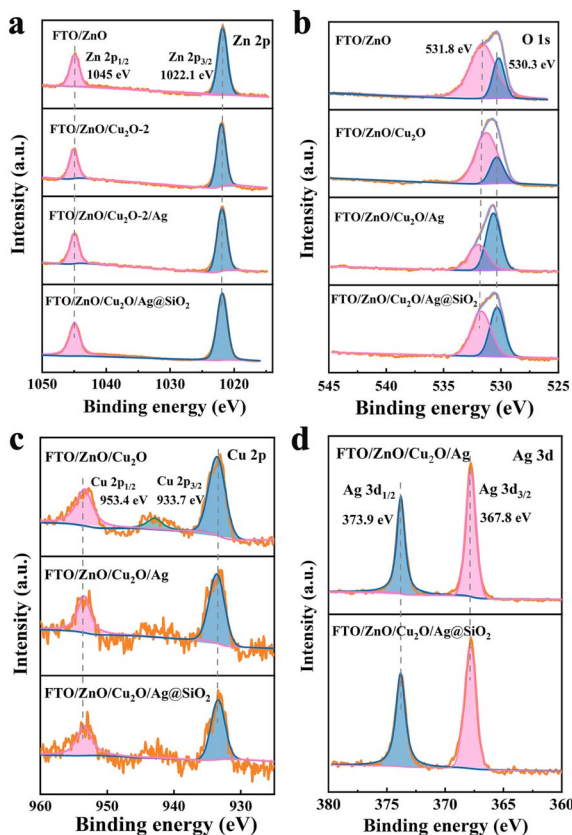
Fig. 2 The XPS spectra of (a) Zn 2p, (b) O 1s in FTO/ZnO, FTO/ZnO/
$Cu_2O$, FTO/ZnO/$Cu_2O$/Ag and FTO/ZnO/$Cu_2O$/Ag@$SiO_2$ photo-
anodes. The XPS spectra of (c) Cu 2p in FTO/ZnO/$Cu_2O$, FTO/ZnO/
$Cu_2O$/Ag and FTO/ZnO/$Cu_2O$/Ag@$SiO_2$ photoanodes. The XPS
spectra of (d) Ag 3d in FTO/ZnO/$Cu_2O$/Ag and FTO/ZnO/$Cu_2O$/
Ag@$SiO_2$ photoanodes.



Fig. 3 The (a) $J–V$ curves, (b) Transient photocurrent density curves,
(c) Nyquist plots at 1.23 $V_{RHE}$ and (d) Mott−Schottky plots of FTO/ZnO,
FTO/ZnO/$Cu_2O$-1, FTO/ZnO/$Cu_2O$-2 and FTO/ZnO/$Cu_2O$-3
photoanodes.

study the effect of $Cu_2O$ and deposition circle on the separation and transfer efficiency of photogenerated carrier in the ZnO photoanodes (Fig. 3). $J–V$ curves are measured using linear scanning voltammetry (Fig. 3a). The photocurrent density of ZnO photoanodes modified with $Cu_2O$ is larger than that of the FTO/ZnO photoanode, where the photocurrent density first increases and then decreases with the deposition circles increases. The small peak at 0.4 $V_{RHE}$ may be caused by the reaction between the ZnO film and NaOH solution, in which the photocurrent density increases much slow with the increasing potential. When the applied potential is far below 0.4 $V_{RHE}$, the water-oxidation dynamics limits the photocurrent density. While close to or over 0.4 $V_{RHE}$, the photogenerated carrier can be efficiently separated and transferring into the electrolyte. The enhancement of photocurrent density is significantly slower as the applied potential is greater than 0.8 $V_{RHE}$, which is possibly due to the limitation of light absorbance for ZnO photoanodes.[24] The excessively low photogenerated carrier separation efficiency may enlarge the effect of side reaction in the $J–V$ curve. The FTO/ZnO/$Cu_2O$-2 photoanode exhibits the best photocurrent density of 0.67 mA $cm^{-2}$ at 1.23 $V_{RHE}$. Thus, the introduction of p–n heterojunction can effectively improve the photocurrent density of ZnO photoanode to achieve a better
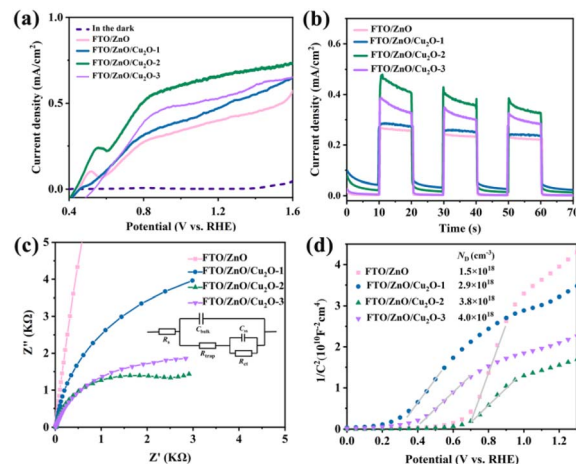
PEC-WS performance.[31] The change trends of transient photocurrent density for FTO/ZnO, FTO/ZnO/$Cu_2O$-1, FTO/ZnO/$Cu_2O$-2, and FTO/ZnO/$Cu_2O$-3 photoanodes are the same as those of the corresponding $J–V$ curves (Fig. 3b), proving that the heterojunction formed between ZnO and $Cu_2O$ can hinder the recombination rate of photogenerated carrier.[32] An equivalent circuit is shown in Fig. 3c, where $R_s$, $R_{trap}$, and $R_{CT}$ represent the series resistance, capture resistance on the surface, and transfer resistance from the surface to the electrolyte, respectively. The arc radii of photoanodes modified with $Cu_2O$ are smaller than that of the pure ZnO photoanode, where the FTO/ZnO/$Cu_2O$-2 photoanode exhibits the smallest arc radius. This implies that the ZnO/$Cu_2O$ p–n heterojunction can effectively decrease the transport resistance to further promote charge transfer.[33] Fig. 3d reveals four different Mott–Schottky curves, where a greater slope implies a smaller donor density. The fitting results show that the slope of FTO/ZnO/$Cu_2O$-2 is the smallest, indicating its largest donor density. These results demonstrate that the FTO/ZnO/$Cu_2O$-2 photoanode possesses the optimal PEC-WS performance. To better study the photoelectrochemical properties of ZnO photoanodes, FTO/ZnO/$Cu_2O$-2 is denoted as FTO/ZnO/$Cu_2O$ photoanode in the following.

To further improve the PEC-WS performance of FTO/ZnO/$Cu_2O$ photoanode, Ag and Ag@$SiO_2$ nanoparticles are introduced to modify its surface. As shown in Fig. 4a, the photocurrent densities of FTO/ZnO/$Cu_2O$/Ag and FTO/ZnO/$Cu_2O$/Ag@$SiO_2$ photoanodes at 1.23 $V_{RHE}$ are significantly greater than that of FTO/ZnO/$Cu_2O$ photoanode. The FTO/ZnO/$Cu_2O$/Ag@$SiO_2$ photoanode exhibits the largest photocurrent density of 0.77 mA $cm^{-2}$ at 1.23 $V_{RHE}$, which is 1.15 times that of FTO/ZnO/$Cu_2O$ photoanode, which is mainly due to that the surface plasmonic effect of Ag@$SiO_2$ nanoparticles effectively promote photogenerated carrier transfer.[34] When Ag@$SiO_2$ plasmonic micitons metal nanostructures are adjacent to ZnO semiconductors to form composite plasmonic micitons metal/semiconductor photocatalysts, this relaxation process will be
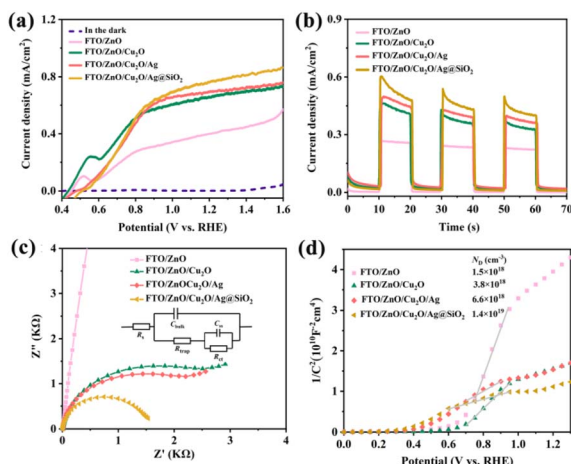
Fig. 4 The (a) $J-V$ curves, (b) transient photocurrent density curves, (c) Nyquist plots at 1.23 $V_{RHE}$ and (d) Mott−Schottky plots of FTO/ZnO, FTO/ZnO/Cu$_2$O, FTO/ZnO/Cu$_2$O/Ag and FTO/ZnO/Cu$_2$O/Ag@SiO$_2$ photoanodes.

effectively extended. This is mainly due to that the plasmon-excited thermal electrons can be injected into the semiconductor from the nanostructures to further enhance the photocatalytic performance.[35–37]

A comparison of PEC-WS performances between ZnO photoanodes in the related literature and our present FTO/TiO$_2$/Cu$_2$O/Ag@SiO$_2$ photoanode is shown in Table S1,† indicating that it possesses a relative better PEC-WS performance.[38–41] The comparison result also indicates that the Cu$_2$O film and Ag@SiO$_2$ catalysts possess a remarkable catalytic effect on the PEC-WS performance of ZnO photoanodes.[42–44] The photostability data of FTO/ZnO/Cu$_2$O/Ag@SiO$_2$ photoanode are provided. The photocurrent shows a drastic decrease at the beginning illumination and an increasing decay with continuous illumination (Fig. S7†). After the stability testing, $J–t$ curves show a certain decrease in photocurrent density due to the gradual corrosion of Cu$_2$O and Ag@SiO$_2$ from the ZnO photoanode (Fig. S8 and S9†). The corresponding XRD patterns (Fig. S10†) prove that there is no obvious change in chemical structure in the ZnO photoanode before and after the stability test.[45]
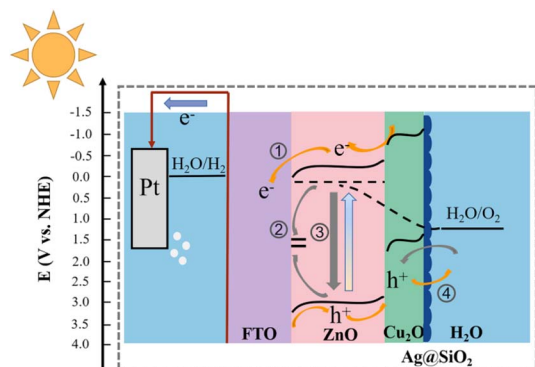
The variation tendencies of transient current density for FTO/ZnO/Cu$_2$O, FTO/ZnO/Cu$_2$O/Ag, and FTO/ZnO/Cu$_2$O/Ag@SiO$_2$ photoanodes are consistent with those of the $J–V$ curves (Fig. 4b).

The transient photocurrent densities of FTO/ZnO/Cu$_2$O/Ag and FTO/ZnO/Cu$_2$O/Ag@SiO$_2$ decrease significantly because of the oxidation of Ag and Ag@SiO$_2$ during the photoelectrochemical process.[45] As shown in Fig. 4c, the FTO/ZnO/Cu$_2$O/Ag@SiO$_2$ photoanode possesses the smallest arc radius, indicating that the introduction of Ag@SiO$_2$ catalyst can decrease the charge transfer resistance to accelerate the photogenerated carrier transfer.[46] The four different Mott–Schottky curves in Fig. 4d also demonstrate that the FTO/ZnO/Cu$_2$O/Ag@SiO$_2$ photoanode has the smallest slope and highest donor density, implying that the introduction of Ag@SiO$_2$ catalyst improves the photogenerated carrier transport.[47]

Fig. 5 shows a schematic diagram of carrier transport for the FTO/ZnO/Cu$_2$O/Ag@SiO$_2$ photoanode in the PEC-WS process. Upon illumination, the photogenerated holes in the Cu$_2$O move toward the Cu$_2$O/electrolyte interface and oxidize water to produce oxygen, and the photogenerated electrons in ZnO move toward to Pt counter electrode by circuit connection to produce hydrogen. The band alignment characteristics at the p–n junction between ZnO and Cu$_2$O can produce photovoltage, and help to reduce the loss of holes in the Cu$_2$O. The p–n heterojunction can improve the electron separation from the hole, and the Ag@SiO$_2$ nanoparticles at the surface can suppress the surface recombination and also facilitate the oxidation reaction.[48] The carrier transport of ZnO photoanode contains four processes: (1) photogenerated electron transfer, (2) bottom surface recombination, (3) bulk recombination, and (4) photogenerated hole transfer.[49,50] After introducing the Cu$_2$O and Ag@SiO$_2$ catalysts on the surface of ZnO, the total amount of photogenerated carrier remains almost unchanged.[51,52] The photogenerated electrons and holes of FTO/ZnO/Cu$_2$O/Ag@SiO$_2$ photoanode are excited when irradiated. Based on the formation of p–n heterojunctions and Ag@SiO$_2$ nanoparticles, the photogeneration of electrons improves (1) due to the decreased bottom surface recombination (2), the bulk recombination process was significantly weakened due to the improved conductivity (3), the surface transfer efficiency of photogenerated carrier is improved based on the internal electric field and surface catalysis (4).

## Conclusions

In this study, a serial of nanosheet-like FTO/ZnO photoanodes are prepared modified with the Cu$_2$O and Ag@SiO$_2$ nanoparticles, where a Cu$_2$O/ZnO p–n heterojunction is formed on the surface of ZnO to promote photogenerated carrier transfer. The photocurrent density of FTO/ZnO/Cu$_2$O/Ag@SiO$_2$ is 0.77 mA cm$^{-2}$ at 1.23 $V_{RHE}$, which is 1.88 times that of the pure ZnO photoanode. Photoelectrochemical analyses demonstrate that a p–n heterojunction formed between ZnO and Cu$_2$O can effectively improve the photogenerated carrier transfer efficiency. The introduction of Cu$_2$O and Ag@SiO$_2$ catalysts significantly enhances the absorbance intensity of FTO/ZnO/



Fig. 5 Schematic diagram of carrier transports in FTO/ZnO/Cu$_2$O/Ag@SiO$_2$ photoanode.

$Cu_2O/Ag@SiO_2$ photoanode. The p–n heterojunction between ZnO and $Cu_2O$ and plasmonic effect of $Ag@SiO_2$ nanoparticles synergistically promote the transfer efficiency of photo-generated carrier. This study provides an insight for designing the nanostructures of semiconductor materials for high PEC-WS performances.

## Conflicts of interest

There are no conflicts to declare.

## Acknowledgements

## Notes and references

1 X.-S. Xing, X. Zeng, Z. Zhou, Z. M. El-Bahy, M. H. Helal, Q. Gao, H. Algadi, P. Song, X. Liu, X. Zhang and J. Du, *Adv. Compos. Hybrid Mater.*, 2023, **6**, 194.

2 S. Chandrasekaran, L. Yao, L. Deng, C. Bowen, Y. Zhang, S. Chen, Z. Lin, F. Peng and P. Zhang, *Chem. Soc. Rev.*, 2019, **48**, 4178–4280.

3 S. Chandrasekaran, C. Bowen, P. Zhang, Z. Li, Q. Yuan, X. Ren and L. Deng, *J. Mater. Chem. A*, 2018, **6**, 11078–11104.

4 N. D. Quang, P. C. Van, D. D. Le, S. Majumder, N. D. Chinh, J.-R. Jeong, C. Kim and D. Kim, *Appl. Surf. Sci.*, 2021, **558**, 149898.

5 Z. Yu, H. Gong, J. Xu, Y. Li, Y. Zeng, X. Liu and D. Tang, *Anal. Chem.*, 2022, **94**, 3418–3426.

6 D. Chen, Z. Liu, Z. Guo, W. Yan and M. Ruan, *Chem. Eng. J.*, 2020, **381**, 122655.

7 P. Peerakiatkhajohn, J.-H. Yun, T. Butburee, M. Lyu, C. Takoon and S. Thaweesak, *RSC Adv.*, 2023, **13**, 18974–18982.

8 X.-S. Xing, Z. Zhou, P. Song, X. Song, X. Ren, D. Zhang, X. Zeng, Y. Guo and J. Du, *Dalton Trans.*, 2023, **52**, 12308–12317.

9 X. Xing, X. Zeng, Z. Zhou, X. Song, X. Jing, M. Yuan, X. Xu, X. Ren and J. Du, *Dalton Trans.*, 2023, **52**, 11203–11212.

10 X. Ren, X. Zeng, Y. Wang, X. Liu, A. Li, X.-S. Xing and J. Du, *ChemistrySelect*, 2022, **7**, e202203608.

11 D. Bu, M. Batmunkh, Y. Zhang, Y. Li, B. Qian, Y. Lan, X. Hou, S. Li, B. Jia, X.-M. Song and T. Ma, *Chem. Eng. J.*, 2022, **433**, 133559.

12 Z. Zhou, S. Wu, C. Xiao, L. Li, W. Shao, H. Ding, L. Wen and X. Li, *Dalton Trans.*, 2019, **48**, 15151–15159.

13 Z. Hu, R. Wang, C. Han and R. Chen, *J. Colloid Interface Sci.*, 2022, **628**, 946–954.

14 T. Tanaka, R. Tsutsumi, T. Yoshinaga, T. Sonoyama, K. Saito, Q. Guo and S. Ikeda, *RSC Adv.*, 2023, **13**, 575–580.

15 W. He, L. Liu, T. Ma, H. Han, J. Zhu, Y. Liu, Z. Fang, Z. Yang and K. Guo, *Appl. Catal., B*, 2022, **306**, 121107.

16 L. Zhang, G. Wang, X. Hao, Z. Jin and Y. Wang, *Chem. Eng. J.*, 2020, **395**, 125113.

17 Z. Zhou, F. Wang, P. Liang, L. Yang, Y. Yu, L. Li, Y. Guo and S. Wu, *ACS Appl. Energy Mater.*, 2022, **5**, 8999–9008.

18 Z. Zhou, Y. Liang, X.-S. Xing, K. Zhang, Y. Niu, L. Yang, F. Wang, Z. Guo, H. Song and S. Wu, *Adv. Compos. Hybrid Mater.*, 2023, **6**, 94.

19 A. P. Sulaeman, R. A. Pratama, U. Pratomo, Irkham, A. S. Matharu and I. Primadona, *RSC Adv.*, 2023, **13**, 18396–18403.

20 C. Li, S. Chen, Y. Wang and Z. Hou, *Int. J. Hydrogen Energy*, 2019, **44**, 25416–25427.

21 D. Maity, K. Karmakar, D. Pal, S. Saha, G. G. Khan and K. Mandal, *ACS Appl. Energy Mater.*, 2021, **4**, 11599–11608.

22 X. Gao, S. Wu, J. Yan, X. Zhai and X. Li, *ACS Appl. Mater. Interfaces*, 2016, **8**, 30072–30078.

23 R. Marschall and L. Wang, *Catal. Today*, 2014, **225**, 111–135.

24 Z. Zhou, Y. Wang, L. Li, L. Yang, Y. Niu, Y. Yu, Y. Guo and S. Wu, *J. Mater. Chem. A*, 2022, **10**, 8546–8555.

25 H. Li, J. Liu, C. Wang, H. Yang and X. Xue, *Vacuum*, 2022, **199**, 110891.

26 S. Yusan, A. Bampaiti, S. Aytas, S. Erenturk and M. A. A. Aslani, *Ceram. Int.*, 2016, **42**, 2158–2163.

27 Y. Li and K. Luo, *RSC Adv.*, 2019, **9**, 8350–8354.

28 E. Mustafa, E. A. Dawi, Z. H. Ibupoto, A. M. M. Ibrahim, A. Elsukova, X. Liu, A. Tahira, R. E. Adam, M. Willander and O. Nur, *RSC Adv.*, 2023, **13**, 11297–11310.

29 T. Narkbuakaem, S. Sattayaporn, N. Asito and P. Sujardworakun, *Appl. Surf. Sci.*, 2022, **573**, 151617.

30 H. Li, H. Liu, F. Wang, G. Li, X. Wang and Z. Tang, *Nano Res.*, 2022, **15**, 5824–5830.

31 B. Wu and N. Zheng, *Nano Today*, 2013, **8**, 168–197.

32 X. Fang, X. Zhao, W. Fang, C. Chen and N. Zheng, *Nanoscale*, 2013, **5**, 2205–2218.

33 Z. Wang, J. Huang, J. Mao, Q. Guo, Z. Chen and Y. Lai, *J. Mater. Chem. A*, 2020, **8**, 2934–2961.

34 H. Peng, F. Liu, X. Liu, S. Liao, C. You, X. Tian, H. Nan, F. Luo, H. Song, Z. Fu and P. Huang, *ACS Catal.*, 2014, **4**, 3797–3805.

35 J.-M. Yi, D. Wang, F. Schwarz, J. Zhong, A. Chimeh, A. Korte, J. Zhan, P. Schaaf, E. Runge and C. Lienau, *ACS Photonics*, 2019, **6**, 2779–2787.

36 C. Tian, D. Jiang, B. Li, J. Lin, Y. Zhao, W. Yuan, J. Zhao, Q. Liang, S. Gao, J. Hou and J. Qin, *ACS Appl. Mater. Interfaces*, 2014, **6**, 2162–2166.

37 X. Wan, J. Liu and J. Zhang, *Small Struct.*, 2022, **3**, 2200045.

38 Z. Peng, S. C. Abbas, J. Lv, R. Yang, M. Wu and Y. Wang, *Int. J. Hydrogen Energy*, 2019, **44**, 2446–2453.

39 S. Zhang, Z. Liu, M. Ruan, Z. Guo, L. E, W. Zhao, D. Zhao, X. Wu and D. Chen, *Appl. Catal., B*, 2020, **262**, 118279.

40 R.-B. Wei, P.-Y. Kuang, H. Cheng, Y.-B. Chen, J.-Y. Long, M.-Y. Zhang and Z.-Q. Liu, *ACS Sustain. Chem. Eng.*, 2017, **5**, 4249–4257.

41 C. Li, S. Chen, Y. Wang and Z. Hou, *Int. J. Hydrogen Energy*, 2019, **44**, 25416–25427.

42 K. Karmakar, A. Sarkar, K. Mandal and G. G. Khan, *Nanotechnology*, 2017, **28**, 325401.

43 S. Xie, W. Wei, S. Huang, M. Li, P. Fang, X. Lu and Y. Tong, *J. Power Sources*, 2015, **2977**, 9–15.

44 D. Maity, K. Karmakar, D. Pal, S. Saha, G. G. Khan and K. Mandal, *ACS Appl. Energy Mater.*, 2021, **4**, 11599–11608.

45 X.-S. Xing, X. Ren, X. Zeng, A. Li, Y. Wang, Z. Zhou, Y. Guo, S. Wu and J. Du, *Sol. RRL*, 2023, **7**, 2201041.

46 L. He, Z. Cui, X. Sun, J. Zhao and D. Wen, *Nanomaterials*, 2022, **12**, 2370.

47 S. Chang, H. Gu, H. Zhang, X. Wang, Q. Li, Y. Cui and W.-L. Dai, *J. Colloid Interface Sci.*, 2023, **644**, 304–314.

48 Z. Zhou, S. Wu, L. Qin, L. Li, L. Li and X. Li, *J. Mater. Chem. A*, 2018, **6**, 15593–15602.

49 X. Xiong, J. Zhang, C. Chen, S. Yang, J. Lin, J. Lin, J. Xi and Z. Kong, *J. Alloys Compd.*, 2022, **926**, 166863.

50 M.-W. Kim, B. Jishi, E. Samuel, H. Samuel, H. Seok, A. Aldabahi, M. Almoiqli, M. T. Swihart and S. S. Yoon, *Appl. Catal., B*, 2020, **271**, 118928.

51 L. Sun, J. Sun, X. Sun, S. Bai, Y. Zhao, R. Luo, D. Li and A. Chen, *J. Colloid Interface Sci.*, 2022, **608**, 2377–2386.

52 X.-S. Xing, M. Bao, P. Wang, X. Wang, Y. Wang and J. Du, *Appl. Surf. Sci.*, 2022, **572**, 151472.